Inorg. Chem. **2008**, *47*, 9919−9929

Crystallographic, Electrochemical, and Electronic Structure Studies of the Mononuclear Complexes of Au(I)/(II)/(III) with [9]aneS$_2$O ([9]aneS$_2$O = 1-oxa-4,7-dithiacyclononane)

Deguang Huang,[†] Xiaofeng Zhang,[†] Eric J. L. McInnes,*[,‡] Jonathan McMaster,*[,†] Alexander J. Blake,[†] E. Stephen Davies,[†] Joanna Wolowska,[‡] Claire Wilson,[†] and Martin Schröder*[,†]

School of Chemistry, University of Nottingham, Nottingham NG9 2RD, U.K., and EPSRC Multi-Frequency EPR Center, School of Chemistry, University of Manchester, Manchester M13 9PL, U.K.

Received May 31, 2008

The mononuclear macrocyclic complexes [Au^{I}([9]aneS$_2$O)$_2$]BF$_4$·MeCN **1a**, [Au^{II}([9]aneS$_2$O)$_2$](BF$_4$)$_2$·2MeCN **2a**, and [Au^{III}([9]aneS$_2$O)$_2$](ClO$_4$)$_6$(H$_5$O$_2$)(H$_3$O)$_2$ **3** ([9]aneS$_2$O = 1-oxa-4,7-dithiacyclononane) have been prepared and structurally characterized by single crystal X-ray crystallography. The oxidation of [Au([9]aneS$_2$O)$_2$]$^{+}$ to [Au([9]aneS$_2$O)$_2$]$^{2+}$ involves a significant reorganization of the co-ordination sphere from a distorted tetrahedral geometry in [Au([9]aneS$_2$O)$_2$]$^{+}$ [Au−S 2.3363(12), 2.3877(12), 2.6630(11), 2.7597(13) Å] to a distorted square-planar co-ordination geometry in [Au([9]aneS$_2$O)$_2$]$^{2+}$. The O-donors in [Au([9]aneS$_2$O)$_2$]$^{2+}$ occupy the axial positions about the Au^{II} center [Au···O = 2.718(2) Å] with the S-donors occupying the equatorial plane [Au−S 2.428(8) and 2.484(8) Å]. [Au([9]aneS$_2$O)$_2$]$^{3+}$ shows a co-ordination sphere similar to that of [Au([9]aneS$_2$O)$_2$]$^{2+}$ but with significantly shorter axial Au···O interactions [2.688(2) Å] and equatorial Au−S bond lengths [2.340(4) and 2.355(6) Å]. The cyclic voltammogram of **1** in MeCN (0.2 M NBu$_4$PF$_6$, 253 K) at a scan rate of 100 mV s^{-1} shows an oxidation process at E_p^a = +0.74 V and a reduction process at E_p^c = +0.41 V versus Fc^{+}/Fc assigned to the two-electron Au$^{III/I}$ couple and a second reduction process at E_p^c = +0.19 V assigned to the Au$^{I/0}$ couple. This electrochemical assignment is confirmed by coulometric and UV−vis spectroelectrochemical measurements. Multifrequency EPR studies of the mononuclear Au^{II} complex [Au([9]aneS$_2$O)$_2$]$^{2+}$ in a fluid solution at X-band and as frozen solutions at L-, S-, X-, K-, and Q-band reveal g_{iso} = 2.0182 and A_{iso} = −44 × 10^{-4} cm^{-1}; g_{xx} = 2.010, g_{yy} = 2.006, g_{zz} = 2.037; A_{xx}= −47 × 10^{-4} cm^{-1}, A_{yy} = −47 × 10^{-4} cm^{-1}, A_{zz} = −47 × 10^{-4} cm^{-1}; P_{xx} = −18 × 10^{-4} cm^{-1}, P_{yy} = −10 × 10^{-4} cm^{-1}, and P_{zz} = 28 × 10^{-4} cm^{-1}. DFT calculations predict a singly occupied molecular orbital (SOMO) with 27.2% Au 5d$_{xy}$ character, consistent with the upper limit derived from the uncertainties in the ^{197}Au hyperfine parameters. Comparison with [Au([9]aneS$_3$)$_2$]$^{2+}$ reveals that the nuclear quadrupole parameters, P_{ii} (i = x, y, z) are very sensitive to the nature of the Au^{II} co-ordination sphere in these macrocyclic complexes. The observed geometries and bond lengths for the cations [Au([9]aneS$_2$O)$_2$]$^{+/2+/3+}$ reflect the preferred stereochemistries of d^{10}, d^{9}, and d^{8} metal ions, respectively, with the higher oxidation state centers being generated at higher anodic potentials compared to the related complexes [Au([9]aneS$_3$)$_2$]$^{+/2+/3+}$.

Introduction

In contrast to complexes of Au^{I} and Au^{III},[1−3] mononuclear Au^{II} complexes remain rare with compounds such as (*n*-Bu$_4$N)$_2$[Au(mnt)$_2$] (mnt = maleonitriledithiolate),[4−8] (*n*-Bu$_4$N)$_2$[Au(dmit)$_2$] (dmit = dimercaptoisotrithione),[9] [Au-

* To whom correspondence should be addressed. E-mail: eric.mciness@man.ac.uk (E.J.L.M.), j.mcmaster@nottingham.ac.uk (J.M.), m.schroder@nottingham.ac.uk (M.S.).
† University of Nottingham.
‡ University of Manchester.

(1) Laguna, A.; Laguna, M. *Coord. Chem. Rev.* **1999**, *193−195*, 837–856.
(2) Puddephatt, R. J. , In *Comprehensive Coordination Chemistry*, Wilkinson, G.; Gillard, R.; McCleverty, J., Eds.; Pergamon Press: Oxford; Vol. *5*, p 861.
(3) Puddephatt, R. J. *The Chemistry of Gold.*; Elsevier: Amsterdam, 1978.
(4) Ihlo, L.; Olk, R. M.; Böttcher, R.; Kirmse, R. *Inorg. Chim. Acta* **1998**, *281*, 160–164.
(5) Kirmse, R.; Kampf, M.; Olk, R. M.; Hildebrand, M.; Krautscheid, H. *Z. Anorg. Allg. Chem.* **2004**, *630*, 1433–1436.
(6) Schlupp, R. L.; Maki, A. H. *Inorg. Chem.* **1974**, *13*, 44–51.

10.1021/ic8010037 CCC: $40.75
Published on Web 10/02/2008

$(dtc)_2]$ (dtc = dithiocarbamate),[10,11] and $[Au(abt)_2]_2$ (abt = *o*-aminobenzenethiol)[12] being better described as ligand-based radical species with significant delocalization of the unpaired electron into ligand-based orbitals.[4−14] In 1990, a genuine mononuclear Au^{II} complex $[Au([9]aneS_3)_2](BF_4)_2 \cdot 2MeCN$ was synthesized and characterized; the X-ray crystal structure of this complex shows that the cation $[Au([9]aneS_3)_2]^{2+}$ possesses C_i symmetry in which six S-thioether donors co-ordinate to the Au^{II} center in a distorted octahedral geometry.[15] Subsequent multifrequency electron paramagnetic resonance (EPR) studies of this complex at L-, S-, X-, K- and Q-band frequencies, together with supporting density-functional theory (DFT) calculations, revealed that this complex possesses a singly occupied molecular orbital (SOMO) with 30% Au character.[16] These multifrequency EPR spectroscopic studies were essential to resolve the spin Hamiltonian parameters associated with the large ^{197}Au nuclear quadrupole interaction in $[Au([9]aneS_3)_2]^{2+}$. This interaction plays a dominant role in determining the relative spacing and intensities of the $\Delta m_I = 0$ hyperfine transitions in $[Au([9]aneS_3)_2]^{2+}$.[16]

Thioether macrocyclic ligands are known to have an affinity for soft transition metal ions[17,18] and the nine-membered macrocycle [9]aneS$_3$ ([9]aneS$_3$ = 1,4,7-trithiacyclononane) is capable of adopting a range of co-ordination modes to accommodate a range of transition metal stereochemistries.[19−21] As part of our ongoing studies of complexes containing unusual metal oxidation states[16,22−26] we were interested in defining the extent to which homoleptic thioether co-ordination stabilizes Au^{I}, Au^{II}, and Au^{III} centers. Thus, we modified the ligand donor set from S_3 to S_2O via incorporation of an ether O-donor in [9]aneS$_2$O ([9]aneS$_2$O = 1-oxa-4,7-dithiacyclononane) and report herein the results of structural and electronic investigations of $[Au([9]aneS_2O)_2]^+$, $[Au([9]aneS_2O)_2]^{2+}$, and $[Au([9]aneS_2O)_2]^{3+}$ as their PF_6^-, BF_4^- and ClO_4^- salts, respectively, allowing direct comparisons with their $[Au([9]aneS_3)_2]^{+/2+/3+}$ analogues.[15,16] We were especially interested in the effect of the change in the co-ordination sphere on the EPR spectroscopic properties, and on the nuclear quadrupole interaction in particular.

Experimental Section

Chemicals. All chemicals were purchased from Aldrich Chemical Co. except for tetrafluoroboric acid (Alfa Aesar). Unless otherwise stated, commercial grade chemicals were used without further purification. MeCN for the electrochemical experiments was freshly distilled from CaH_2 under an atmosphere of N_2, and NBu_4PF_6 (Fluka, Electrochemical grade) was dried before use. The macrocyclic ligand, [9]aneS$_2$O,[27] and $[Au^I(tht)_2]PF_6$[28] (tht = tetrahydrothiophene) were prepared by literature methods. **Caution!** *perchlorate salts may be explosive when heated.*

Physical Measurements. ^1H NMR spectra were recorded on a Bruker DPX300 instrument operating at 300 MHz. Infrared spectra were recorded with a Nicolet Avatar 360 FT-IR spectrometer. UV−vis spectra were recorded on a Perkin-Elmer Lambda 16 spectrophotometer. Fast Atom Bombardment (FAB) and Electron Impact (EI) mass spectra were run on Micromass Autospec mass spectrometer. Elemental analyses were performed by the Microanalytical Service at the University of Nottingham with an Exeter Analytical Inc. CE-440 Elemental analyzer. Cyclic voltammetric and coulometric studies were carried out on an Autolab PGSTAT20 potentiostat. Cyclic voltammetry was carried out on 10^{-3} M solutions of the complexes under an atmosphere of Ar. A single compartmental cell was used with glassy-carbon, Pt wire, and saturated calomel functioning as the working, counter, and reference electrodes, respectively. All potentials are quoted versus the ferrocenium-ferrocene couple.[29] Coulometry was conducted in a two-compartment cell using a Pt/Rh gauze basket working electrode separated from a wound Pt/Rh gauze secondary electrode by a glass frit. UV−vis spectroelectrochemical experiments were carried out under potential control by a Sycopel Scientific Ltd. DD10 M potentiostat using a Pt/Rh gauze as working electrode in an optically transparent electrochemical (OTE) cell ($40 \times 10 \times 0.5$ mm^3).[30] Multifrequency EPR spectra were recorded on Bruker ESP 300E (L-, S-, K-, Q-band) and Bruker EMX EPR (X-band) spectrometers, respectively. Simulations of the fluid and frozen spectra were

(7) van Rens, J. G. M.; de Boer, E. *Mol. Phys.* **1970**, *19*, 745–747.
(8) Waters, J. H.; Gray, H. B. *J. Am. Chem. Soc.* **1965**, *87*, 3534–3535.
(9) Ihlo, L.; Olk, R. M.; Kirmse, R. *Inorg. Chem.* **2001**, *40*, 626–628.
(10) van Willigen, H.; van Rens, J. G. M. *Chem. Phys. Lett.* **1968**, *2*, 283–285.
(11) Vängård, T. S.; Åkerström, S. *Nature* **1959**, *184*, 183–184.
(12) Koley, A. P.; Purohit, S.; Ghosh, S.; Praad, L. S.; Manoharan, P. T. *J. Chem. Soc., Dalton Trans.* **1988**, 2607–2613.
(13) Koley, A. P.; Praad, L. S.; Manoharan, P. T.; Ghosh, S. *Inorg. Chim. Acta* **1992**, *194*, 219–225.
(14) Koley, A. P.; Purohit, S.; Ghosh, S.; Prasad, L. S.; Manoharan, P. T. *Inorg. Chem.* **1992**, *31*, 305–311.
(15) Blake, A. J.; Greig, J. A.; Holder, A. J.; Hyde, T. I.; Taylor, A.; Schröder, M. *Angew. Chem., Int. Ed. Engl.* **1990**, *29*, 197–198.
(16) Shaw, J. L.; Wolowska, J.; Collison, D.; Howard, J. A. K.; McInnes, E. J. L.; McMaster, J.; Blake, A. J.; Wilson, C.; Schröder, M. *J. Am. Chem. Soc.* **2006**, *128*, 13827–13839.
(17) (a) Reid, G.; Schröder, M. *Chem. Soc. Rev.* **1990**, *19*, 239–269. (b) Blake, A. J; Reid, G.; Schröder, M. *J. Chem. Soc., Chem. Commun.* **1992**, 1074–1076. (c) Blake, A. J.; Gould, R. O.; Reid, G.; Schröder, M. *J. Chem. Soc., Chem. Commun.* **1990**, 974–976.
(18) Blake, A. J.; Schröder, M. *Adv. Inorg. Chem.* **1990**, *35*, 1–81.
(19) (a) Schröder, M. *Pure Appl. Chem.* **1988**, *60*, 517–524. (b) Blake, A. J.; Holder, A. J.; Hyde, T. I.; Küppers, H-J.; Schröder, M.; Stötzel, S.; Wieghardt, K. *J. Chem. Soc., Chem. Commun.* **1989**, 1600–1602. (c) Blake, A. J.; Holder, A. J.; Hyde, T. I.; Schröder, M. *J. Chem. Soc., Chem. Commun.* **1989**, 1433–1434.
(20) Blake, A. J.; Gould, R. O.; Greig, J. A.; Holder, A. J.; Hyde, T. I.; Schröder, M. *J. Chem. Soc., Chem. Commun.* **1989**, 876–878.
(21) Bell, M. N.; Blake, A. J.; Gould, R. O.; Holder, A. J.; Hyde, T. I.; Lavery, A. J.; Reid, G.; Schröder, M. *J. Inclusion Phenom.* **1987**, *5*, 169–172.
(22) (a) Ansell, C. W.; Lewis, G. J.; Raithby, P. R.; Ramsden, J. N.; Schröder, M. *J. Chem. Soc., Chem. Commun.* **1982**, 546–547. (b) Lewis, J.; Schröder, M. *J. Chem. Soc., Dalton Trans.* **1982**, 1085–1089.
(23) Blake, A. J.; Gould, R. O.; Hyde, T. I.; Schröder, M. *J. Chem. Soc., Chem. Commun.* **1987**, 431–433.
(24) Blake, A. J.; Holder, A. J.; Hyde, T. I.; Schröder, M. *J. Chem. Soc., Chem. Commun.* **1989**, 1433–1434.
(25) Blake, A. J.; Reid, G.; Schröder, M. *J. Chem. Soc., Dalton Trans.* **1990**, 3363–3373.
(26) (a) Wang, Q.; Barclay, E.; Blake, A. J.; Davies, E. S.; Evans, D. J.; Marr, A. C.; McInnes, E. J. L.; McMaster, J.; Wilson, C.; Schröder, M. *Chem.−Eur. J.* **2004**, *10*, 3384–3396. (b) Stenson, P. A.; Board, A.; Marin-Becerra, A.; Blake, A. J.; Davies, E. S.; Wilson, C.; McMaster, J.; Schröder, M. *Chem.−Eur. J.* **2008**, *14*, 2564–2576.
(27) Grant, G. J.; Galas, D. F.; Jones, M. W.; Loveday, K. D.; Pennington, W. T.; Schimek, G. L.; Eagle, C. T.; VanDerveer, D. G. *Inorg. Chem.* **1998**, *37*, 5299–5305.
(28) Usón, R.; Laguna, A.; Navarro, A.; Parish, R. V.; Moore, L. S. *Inorg. Chim. Acta* **1986**, *112*, 205–208.
(29) Gagné, R. R.; Koval, C. A.; Lisensky, G. C. *Inorg. Chem.* **1980**, *19*, 2854–2855.
(30) Macgregor, S. A.; McInnes, E. J. L. ; Sorbie, R. J.; Yellowlees, L. J. In *Molecular Electrochemistry of Inorganic, Bioinorganic and Organometallic Compounds*; Pombeiro, A., McCleverty, J., Eds.; Kluwer Academic Publishers: Norwell, MA, 1993; p 503.

Table 1. Crystallographic Data for Complexes **1a**, **2a**, and **3**

complex	**1a**	**2a**	**3**
chemical formula	$C_{14}H_{27}S_4O_2NBF_4Au$	$C_{16}H_{30}S_4O_2N_2B_2F_8Au$	$C_{12}H_{35}S_4O_{30}Cl_6Au$
M	653.38	781.25	1197.31
crystal color	colorless	red	yellow
crystal system	monoclinic	monoclinic	monoclinic
space group	$P2_1/n$	$P2_1/n$	$P2_1/c$
a/Å	7.6234(6)	7.6982(7)	10.3040(8)
b/Å	19.639(2)	8.5629(8)	8.8752(7)
c/Å	14.7970(13)	20.190(2)	19.4609(15)
β/deg	102.147(2)	92.385(2)	95.881(1)
V/Å^3	2165.7(3)	1329.75(17)	1770.3(2)
Z	4	2	2
μ/mm^{-1}	7.222	5.920	4.952
T/K	150(2)	150(2)	150(2)
unique data	5009	3246	4294
observed data [$F \geq 4\sigma(F)$]	3831	2535	3752
refined parameters	245	161	263
R_1, wR_2 [$F \geq 4\sigma(F)$]	0.0354, 0.0726	0.0218, 0.0513	0.0269, 0.0700
R_1, wR_2 (all data)	0.0518, 0.0796	0.0292, 0.0553	0.0290, 0.0713

performed using the SimFonia package[31] and the commercial XSophe software,[32] respectively.

Synthesis. [Au([9]aneS$_2$O)$_2$]PF$_6$·CH$_2$Cl$_2$ (1). Solutions of 1-oxa-4,7-dithiacyclononane (62 mg, 0.38 mmol) in CH_2Cl_2 (1 mL), [Au(tht)$_2$]PF$_6$ (96 mg, 0.19 mmol) in CH_2Cl_2 (1 mL) and Et_2O (4 mL) were layered from bottom to top in a thin tube. The sealed tube was stored at −20 °C for 3 days, after which time colorless blocky crystals of **1** deposited, yield 72 mg, 50%. Anal. Calcd for $C_{13}H_{26}S_4O_2Cl_2PF_6Au$: C, 20.66; H, 3.44. Found: C, 20.81; H, 3.33. M.S. *m*/*z* (FAB): 525 for [Au([9]aneS$_2$O)$_2$]$^+$ and 361 for [Au([9]aneS$_2$O)]$^+$ with correct isotopic distributions. IR (KBr, cm^{-1}): 2907, 2858, 1468, 1409, 1351, 1294, 1272, 1235, 1215, 1122, 1107, 1008, 921, 864−819 (broad, s), 731, 557.

[Au([9]aneS$_2$O)$_2$](BF$_4$)$_2$ (2). 1-Oxa-4,7-dithiacyclononane (109 mg, 0.66 mmol) and aqueous 25% HBF_4 (14 mL) were mixed and stirred at room temperature for 40 min. To this solution $HAuCl_4 \cdot 3H_2O$ (159 mg, 0.40 mmol) was added and the mixture stirred for a further 4 min. The solution was filtered to remove a yellow solid and $MeNO_2$ (40 mL) followed by H_2O (80 mL) were added to the red solution. The layers were separated and the aqueous layer washed with $MeNO_2$ (2 × 10 mL). The solvent was removed in vacuo from the combined organic layers to leave a deep-red oil which was dissolved in MeCN (2 mL) and Et_2O (50 mL) added to deposit a brown solid which was collected and dried in vacuo, yield 97 mg, 42%. Anal. Calcd for $C_{12}H_{24}S_4O_2B_2F_8Au$: C, 20.60; H, 3.43. Found: C, 20.16; H, 3.18. M.S. *m*/*z* (FAB): 525 for [Au([9]aneS$_2$O)$_2$]$^+$ and 361 for [Au([9]aneS$_2$O)]$^+$ with the correct isotopic distribution.

Red blocky crystals of [Au([9]aneS$_2$O)$_2$](BF$_4$)$_2$·2MeCN (**2a**) suitable for X-ray crystallography were obtained by the diffusion of Et_2O into a concentrated solution of complex **2** in MeCN at −20 °C. After the deposition of **2a**, a small quantity of colorless, diffraction-quality crystals of [Au([9]aneS$_2$O)$_2$]BF$_4$·MeCN (**1a**) formed from the same solution.

[Au([9]aneS$_2$O)$_2$](ClO$_4$)$_6$(H$_5$O$_2$)(H$_3$O)$_2$ (3). Compound **1** (76 mg, 0.1 mmol) was dissolved in 70% $HClO_4$ (0.5 mL) to give a yellow solution. The solution was stored at −20 °C for a week and yellow block crystals **3** suitable for X-ray diffraction were obtained, yield 20 mg, 17%. UV−vis spectrum (in 70% $HClO_4$) [λ_{max}(ε_{max})]: 233 nm (5900 L mol^{-1} cm^{-1}), 331 (15600).

X-ray Crystallography. Single crystal X-ray diffraction data for **1a**, **2a**, and **3** were collected on Bruker SMART CCD area detector diffractometers equipped with Oxford Cryosystems open-flow nitrogen cryostats. For X-ray diffraction studies, single crystals were coated in a film of perfluoropolyether (Fomblin YR-1800; Lancaster Synthesis), mounted on dual-stage glass fibers and cooled using dry ice during transfer to the diffractometer. Reflection data were collected with Mo $K\alpha$ X-radiation (λ = 0.71073 Å) at 150 K. Structures were solved by direct methods using the SHELXTL program package,[33] and all non-hydrogen atoms were refined with anisotropic displacement parameters. Hydrogen atoms were placed geometrically except for those of water molecules and three protons in **3** where they were located from difference Fourier maps; their positions and displacement parameters were restrained in subsequent refinement. The positions of the water hydrogen atoms in **3** were identified from difference Fourier maps: they are bound to four oxygen atoms to form one $H_5O_2^+$ cation and two H_3O^+ cations. In combination with the previously identified Au^{III} center and six ClO_4^- anions this establishes the required electro-neutrality. Crystal data and refinement details are given in Table 1.

DFT Calculations. Calculations were performed using the Amsterdam Density Functional (ADF) suite version 2005.01.[34,35] The unrestricted DFT calculations employed a Slater type orbital (STO) all-electron triple-ζ-plus one polarization function basis set from the ZORA/TZP database of the ADF suite for all atoms. Scalar relativistic (SR) and spin−orbit coupling (SO) approaches were used within the ZORA Hamiltonian for the inclusion of relativistic effects. The local density approximation (LDA) with the correlation potential due to Vosko et al.[36] was used in all of the DFT calculations. Gradient corrections were performed using the functionals of Becke[37] and Perdew (BP).[38] A model of [Au([9]aneS$_2$O)$_2$]$^{2+}$ in C_i symmetry was constructed using geometrical data from the X-ray crystal structure of **2a**. The co-ordinate frame employed in the calculation is shown in Figure 6a. The *y* axis bisects the S(4)−Au(1)−S(7) angle and the *x*-axis lies in the equatorial AuS$_4$ plane. This model geometry was optimized at the ZORA SR level. The *g*-matrix was obtained from an unrestricted ZORA SO calculation using the collinear approximation on the geometry

(31) *Winepr SimFonia*; Bruker Analytische Messtechnik GmbH: Germany, 1996.
(32) *Xsophe Computer Simulation Suite*; Bruker Biospin GmbH: Germany, 2003.
(33) Sheldrick, G. M. *Acta Crystallogr., Sect. A* **2008**, *64*, 112–122.
(34) Fonseca Guerra, C.; Snijders, J. G.; te Velde, G.; Baerends, E. J. *Theor. Chem. Acc.* **1998**, *99*, 391–403.
(35) te Velde, G.; Bickelhaupt, F. M.; van Gisbergen, S. J. A.; Fonseca Guerra, C.; Baerends, E. J.; Snijders, J. G.; Ziegler, T. *J. Comput. Chem.* **2001**, *22*, 931–967.
(36) Vosko, S. H.; Wilk, L.; Nusair, M. *Can. J. Phys.* **1980**, *58*, 1200–1211.
(37) Becke, A. D. *Phys. Rev. A.* **1988**, *38*, 3098–3100.
(38) Perdew, J. P. *Phys. Rev. B.* **1986**, *33*, 8822–8824.

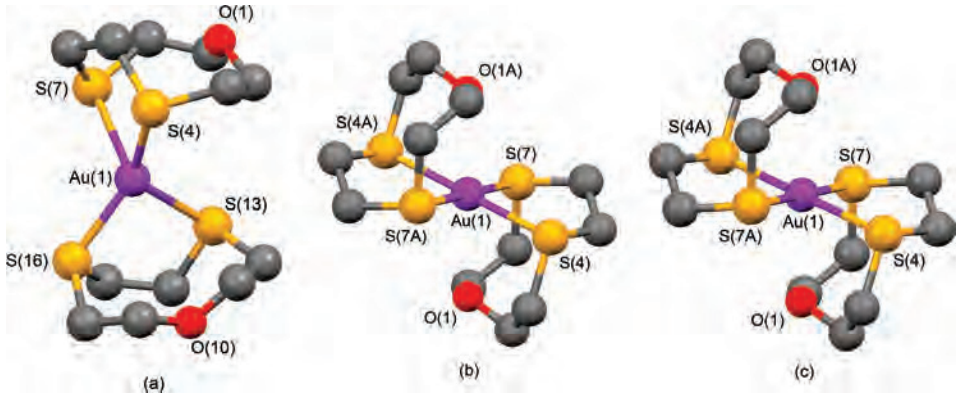

Figure 1. Views of the cations $[Au([9]aneS_2O)_2]^+$ (a) in **1a**, $[Au([9]aneS_2O)_2]^{2+}$ (b) in **2a**, and $[Au([9]aneS_2O)_2]^{3+}$ (c) H atoms are omitted for clarity. Atoms with the suffix A are related to their unsuffixed equivalents by inversion: the symmetry operations are $(2 - x, -y, -z)$ in **2a** and $(1 - x, 1 - y, 1 - z)$ in **3**.

Table 2. Selected Bond Lengths (Å) and Angles (deg) for Complexes **1a**, **2a**, and **3** Derived from X-ray Crystallography and by DFT Calculations for **2a**

1a		**2a**	expt	calc	**3**	
Au(1)···O(1)	3.752(4)	Au(1)···O(1)	2.718(2)	2.876	Au(1)···O(1)	2.688(2)
Au(1)−S(4)	2.336(3)	Au(1)−S(4)	2.428(9)	2.523	Au(1)−S(4)	2.340(5)
Au(1)−S(7)	2.759(7)	Au(1)−S(7)	2.484(9)	2.544	Au(1)−S(7)	2.355(7)
Au(1)···O(10)	3.511(3)					
Au(1)−S(13)	2.663(1)					
Au(1)−S(16)	2.387(7)					
S(4)−Au(1)−S(7)	86.53(4)	S(4)−Au(1)−S(7)	87.64(2)	85.7	S(4)−Au(1)−S(7)	88.73(3)
S(4)−Au(1)−S(13)	125.42(4)					
S(4)−Au(1)−S(16)	144.80(4)					
S(7)−Au(1)−S(13)	100.64(4)					
S(7)−Au(1)−S(16)	105.02(4)					
S(13)−Au(1)−S(16)	85.69(4)					

optimized structure derived from the unrestricted ZORA SR calculation.

Results and Discussion

Syntheses of 1, 2, and 3. Solvent diffusion of a solution of $[Au(tht)_2]PF_6$ in CH_2Cl_2 into a solution of 2 molar equivalents of $[9]aneS_2O$ in CH_2Cl_2 afforded complex **1** as colorless crystals. Mass spectrometric, microanalytical, and IR spectroscopic data confirm the formulation of **1** as $[Au^I([9]aneS_2O)_2]PF_6 \cdot CH_2Cl_2$. Complex **2** was prepared by the reaction of $HAuCl_4 \cdot 3H_2O$ with 2 molar equivalents of $[9]aneS_2O$ in 25% HBF_4 for 4 min at room temperature using similar reaction conditions to those reported previously for the synthesis of $[Au^{II}([9]aneS_3)_2](BF_4)_2$.[15,16] In this reaction $[9]aneS_3$ reduces Au^{III} to Au^{II} to form $[Au^{II}([9]aneS_3)_2]^{2+}$ with the concomitant formation of a bicyclic sulfonium salt;[39] it is likely that $[9]aneS_2O$ behaves similarly in the reaction to form **2**. Mass spectral and microanalytical data are consistent with the formulation $[Au^{II}([9]aneS_2O)_2](BF_4)_2$ for this compound. Oxidation of **1** in 70% $HClO_4$ produces $[Au^{III}([9]aneS_2O)_2](ClO_4)_6(H_5O_2)(H_3O)_2$ (**3**) as yellow blocky crystals. Crystals of $[Au^I([9]aneS_2O)_2]BF_4 \cdot MeCN$ (**1a**) and $[Au^{II}([9]aneS_2O)_2](BF_4)_2 \cdot 2MeCN$ (**2a**) were isolated from the diffusion of Et_2O into a concentrated solution of **2** in MeCN at −20 °C. The isolation of **2a** *and* **1a** from solutions of **2** in MeCN, together with our electrochemical observations detailed below, suggests that **2** and **2a** may undergo disproportionation reactions in MeCN solution to form **1a** and Au^{III} species.

Crystal Structures of 1a, 2a, and 3. The structures of the cations in **1a**, **2a**, and **3** are shown in Figure 1, and selected bond lengths and angles are shown in Table 2. For comparison, views of the structures and bond lengths and angles for the related complexes $[Au([9]aneS_3)_2]^{+/2+/3+}$ are given in Figure 2 and Table 3. The structure of $[Au([9]aneS_2O)_2]^+$ in **1a** (Figure 1a) shows a distorted tetrahedral geometry with the Au^I center bound asymmetrically to four S-donors. The macrocyclic O-donors remain unbound to the Au^I center in an *exo* conformation such that the O-lone pairs are directed away from the metal center. $[Au([9]aneS_3)_2]^+$ also adopts a distorted tetrahedral geometry about the Au^I center.[20] However, the conformations of the macrocyclic ligands about the Au^I centers in **1a** and $[Au([9]aneS_3)_2]^+$ differ significantly. Thus, for $[Au([9]aneS_3)_2]^+$, three S-donors derived from one $[9]aneS_3$ macrocycle adopt an irregular facial co-ordination to the metal center with the fourth S-donor to Au^I in $[Au([9]aneS_3)_2]^+$ coming from a second $[9]aneS_3$ macrocycle whose other two S-donors remain unbound. In contrast, within **1a** two S-donors from each $[9]aneS_2O$ macrocycle bind to the metal center with the O-donors remaining unco-ordinated, a clear reflection of the tendency for soft−soft Lewis acid−base Au^I−S interactions in these compounds. Our studies on **1a** and $[Au([9]aneS^3)_2]^+$ [20] suggest the formation of highly distorted tetrahedral co-ordination spheres, composed of two short and two long Au−S bonds ([2+2]), appears to be a general

(39) Taylor, A.; Blake, A. J.; Holder, A. J.; Hyde, T. I.; Schroder, M. *New J. Chem.*, **1991**, *15*(7), 511−514.

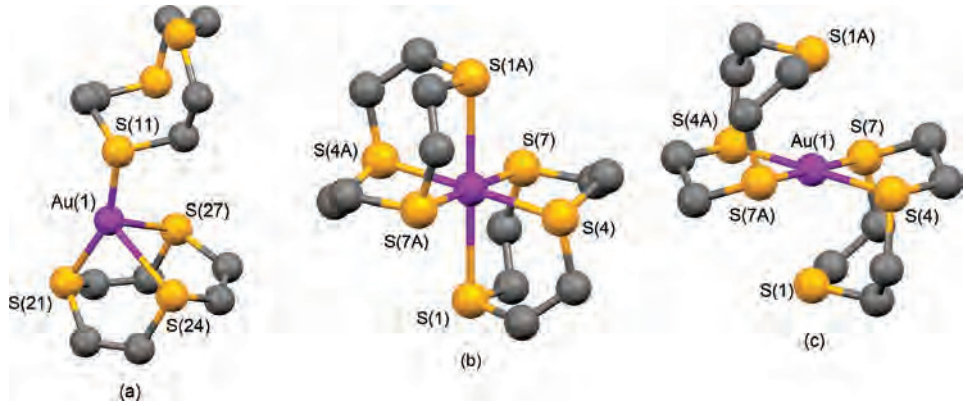

Figure 2. Views of the cations $[Au([9]aneS_3)_2]^{+}$ [20] (a), $[Au([9]aneS_3)_2]^{2+}$ [15] (b), and $[Au([9]aneS_3)_2]^{3+}$ [20] (c) H atoms are omitted for clarity.

Table 3. Selected Bond Lengths (Å) and Angles (deg) for Cations $[Au([9]aneS_3)_2]^{+}$,[20] $[Au([9]aneS_3)_2]^{2+}$,[15] and $[Au([9]aneS_3)_2]^{3+}$[20]

$[Au([9]aneS_3)_2]^{+}$		$[Au([9]aneS_3)_2]^{2+}$		$[Au([9]aneS_3)_2]^{3+}$	
Au(1)−S(11)	2.302(6)	Au(1)−S(1)	2.839(5)	Au(1)···S(1)	2.926(4)
Au(1)−S(21)	2.350(7)	Au(1)−S(4)	2.462(5)	Au(1)−S(4)	2.348(4)
Au(1)−S(24)	2.733(8)	Au(1)−S(7)	2.452(5)	Au(1)−S(7)	2.354(4)
Au(1)−S(27)	2.825(8)				
S(11)−Au(1)−S(21)	154.0(2)	S(4)−Au(1)−S(7)	87.7(2)	S(4)−Au(1)−S(7)	89.60(15)
S(11)−Au(1)−S(24)	113.1(2)	S(1)−Au(1)−S(4)	83.7(2)		
S(11)−Au(1)−S(27)	118.4(2)	S(1)−Au(1)−S(7)	83.6(2)		

structural motif for Au^{I}−crown thioether macrocyclic complexes. $[Au([18]aneS_6)]PF_6$ [Au−S = 2.321(3), 2.320(4), 2.856(4) and 2.870(4) Å; bond angle of 155.93(12)° for the two short Au−S bonds][40] and $[Au_2([28]aneS_8)](PF_6)_2$ [Au−S = 2.330(2), 2.338(2), 2.789(2), and 2.763(2) Å; bond angle of 155.58(6)° for the two short Au−S bonds],[41] also adopt similar [2+2] distorted tetrahedral co-ordination spheres to **1a** and $[Au([9]aneS_3)_2]^{+}$ about each Au^{I} center. This [2+2] distorted tetrahedral co-ordination may be regarded as a compromise between the preferred co-ordination modes of crown thioether macrocyles and the tendency of Au^{I} centers to adopt linear co-ordination modes.

In the crystal structure of **2a** the $[Au([9]aneS_2O)_2]^{2+}$ cation occupies a crystallographic inversion center (Figure 1b), [C_i imposed symmetry] with four S-donors from two [9]aneS_2O rings co-ordinating to the Au^{II} center to form a distorted square-planar geometry. The Au−S bonds are significantly different from each other [Au(1)−S(4) = 2.428(8) and Au(1)−S(7) = 2.484(8) Å] and the S(4)−Au(1)−S(7) angle [87.64(2)°] is significantly less than 90° (Table 2). The two O-donors from each [9]aneS_2O macrocycle occupy approximately axial positions (the Au−O vectors lie 20.2° from the axis perpendicular to the equatorial AuS_4 plane) and remain distant from the Au^{II} center. Thus, the [9]aneS_2O rings in **2a** adopt a conformation similar to that of the free form of the ligand[42] which is significantly different from those conformations adopted in **1a**. The Au−S bond lengths in **2a** are comparable to those observed for the equatorial Au−S bonds in $[Au([9]aneS_3)_2]^{2+}$,[15] although in contrast to **2a** the Au−S bond distances in $[Au([9]aneS_3)_2]^{2+}$ are equivalent within two s.u. The remaining S-donors from each [9]aneS_3 ligand form two long Au−S bonds lying only 8.8° from the axis perpendicular to the equatorial AuS_4 plane in $[Au([9]aneS_3)_2]^{2+}$.

The co-ordination sphere of $[Au([9]aneS_2O)_2]^{3+}$ in **3** (Figure 1c) is similar to that of **2a** but with significantly shorter equatorial Au−S bond lengths and shorter axial Au···O distances (Table 2). A decrease in the angle between the Au−O vectors and the axis perpendicular to the equatorial AuS_4 plane from 20.2° in **2a** to 16.9° in **3** accompanies the contraction of the bonds within the Au^{III} co-ordination sphere in **3**. These observations are all consistent with the increase in the formal charge of the Au^{III} center in **3** relative to that of the Au^{II} center in **2a**. The equatorial Au−S bond distances in **3** are essentially identical to those of 2.348(4) and 2.354(4) Å found in $[Au([9]aneS_3)_2]^{3+}$.[20] However, in contrast to **2a** and **3** where the axial Au···O distance shortens with the increase in formal oxidation state, $[Au([9]aneS_3)_2]^{3+}$ shows a longer axial Au···S distance [2.926(4) Å] than that seen in $[Au([9]aneS_3)_2]^{2+}$ [2.839(5), Å],[15,20] presumably reflecting the greater importance of Au−S axial covalent interactions for the lower oxidation state Au^{II} centers. In addition, the angle between the Au(1)−S(1) vectors to the axis perpendicular to the equatorial AuS_4 plane changes little from $[Au([9]aneS_3)_2]^{2+}$ to $[Au([9]aneS_3)_2]^{3+}$ (8.8 and 8.6°, respectively), in contrast to the corresponding angles in **2a** (20.2°) and **3** (16.9°).

Electrochemical Studies of $[Au([9]aneS_2O)_2]^{+}$. The cyclic voltammogram of **1** in MeCN (0.2 M NBu_4PF_6, 253 K) at a scan rate of 100 mV s^{-1} shows an oxidation process at $E_p^a = +0.74$ V, an associated reduction process at +0.41 V, and a further broad reduction process at $E_p^c = +0.19$ V versus Fc^{+}/Fc (Figure 3). Coulometric measurements at +0.85 V confirm that the oxidation process of **1** is a two-electron transfer step to afford a yellow EPR silent solution consistent with the oxidation of **1** to a Au^{III} species. During the oxidation process, and before 2 reductive equivalents had

(40) Blake, A. J.; Taylor, A.; Schröder, M. *Chem. Commun.* **1993**, 1097–1098.
(41) Blake, A. J.; Li, W. S.; Lippolis, V.; Taylor, A.; Schröder, M. *J. Chem. Soc., Dalton Trans.* **1998**, 2931–2937.
(42) Cooper, S. R. *Acc. Chem. Res.* **1988**, *21*, 41–146.

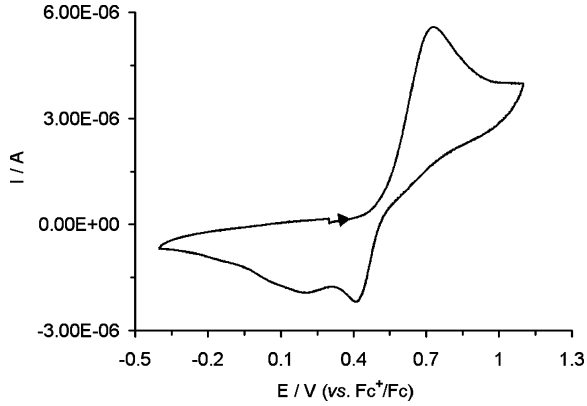

Figure 3. Cyclic voltammogram of **1** in MeCN (0.2 M NBu_4PF_6, 253 K) at a scan rate of 100 mV s^{-1}.

Table 4. Comparison of UV-vis Data and $E_{1/2}$ of Analogous Complexes $[Au([9]aneS_2O)_2]^{n+}$ and $[Au([9]aneS_3)_2]^{n+}$[15,40] (n = 1, 2 and 3) in MeCN

	UV−vis data (nm/L mol^{-1} cm^{-1})	E/V (vs Fc^+/Fc)
$[Au([9]aneS_2O)_2]^+$	225 (6100)	E_p^a = +0.74 V and E_p^c = +0.41 V for Au(I)/Au(III)
$[Au([9]aneS_2O)_2]^{2+}$	405 (2000) and 235 (5500)	
$[Au([9]aneS_2O)_2]^{3+}$	331 (13300) and 238 (6400)	
$[Au([9]aneS_3)_2]^+$	not observed	$E_{1/2}$ = +0.12[c] V for Au(I)/Au(II) and $E_{1/2}$ = +0.46 V for Au(II)/Au(III)[b]
$[Au([9]aneS_3)_2]^{2+}$	398 (7990) and 234 (15000)[a]	
$[Au([9]aneS_3)_2]^{3+}$	334 (19765) and 246 (20265)[a]	

[a] Experiment was run at 293 K. [b] Measured in MeCN (0.1 mol L^{-1} NBu_4PF_6) at 293 K at platinum electrodes at a scan rate of 100 mV s^{-1}. [c] Irreversible.

passed through the solution, a red solution formed. X-band EPR spectroscopic studies at ambient temperature confirmed that this solution contained a paramagnetic species that exhibited an isotropic EPR spectrum, with g_{iso} = 2.0182, which was identical to that of the fluid spectrum of $[Au([9]aneS_2O)_2](PF_6)_2$ chemically generated in MeCN (see below). Bulk reduction at +0.30 V versus Fc^+/Fc of the electrochemically prepared Au^{III} solution generated the same intermediate red species during the reduction to **1**.

The two-electron oxidation of **1** was studied by in situ UV−vis spectroelectrochemistry in MeCN (0.2 M NBu_4PF_6, 253 K) under N_2 to gain further insight into the nature of the species in solution during and after the electrochemical oxidation process (Table 4). The UV-vis spectrum of **1** in MeCN (0.2 M NBu_4PF_6, 253 K) shows a single absorption band at 225 nm (6100 L mol^{-1} cm^{-1}, Figure 4a). The oxidation of **1** at +0.85 V versus Fc^+/Fc was accompanied by the growth of new absorption bands at 331 nm (13300 L mol^{-1} cm^{-1} after oxidation) and 238 nm (6400 L mol^{-1} cm^{-1} after oxidation) together with the loss of the band at 225 nm for **1** (Figure 4a). During the oxidation process an overlapping band at 405 nm was observed to a maximum extinction coefficient of 2000 L mol^{-1} cm^{-1} and then

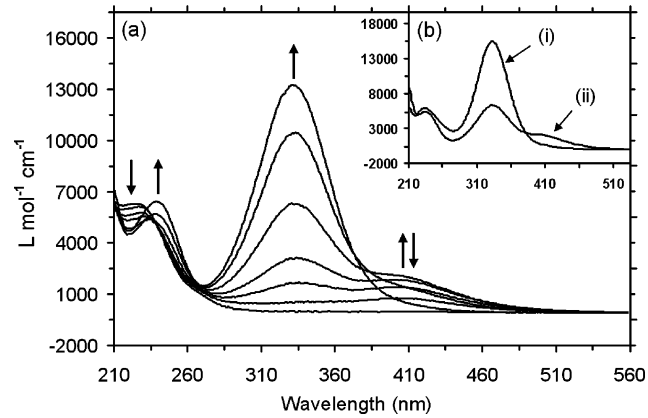

Figure 4. (a) In situ UV-vis spectroelectrochemical data for the two-electron oxidation of **1** at +0.85 V in MeCN (0.2 M NBu_4PF_6, 253 K); (b) electronic spectra of **3** in 70% $HClO_4$ (i) and **2a** in MeCN (ii) at 253 K.

diminished in intensity as the two-electron oxidation of the solution proceeded.

Comparison of the UV-vis spectrum of the electrochemically oxidized solution of **1** with that of **3** prepared by the chemical oxidation of **1** in 70% $HClO_4$ solution (Figure 4b) confirmed the generation of $[Au([9]aneS_2O)_2]^{3+}$ by each route. In addition, the band at 405 nm, associated with an intermediate species during the electrochemical oxidation of **1**, may be assigned to $[Au([9]aneS_2O)_2]^{2+}$ on the basis of comparisons with the UV-vis absorption spectrum of **2** in MeCN (Figure 4b). Furthermore, the original spectrum of **1** can be regenerated by electrochemical reduction at +0.30 V versus Fc^+/Fc of the electrochemically prepared $[Au([9]aneS_2O)_2]^{3+}$ species. This confirmed that the $[Au([9]aneS_2O)_2]^{+/3+}$ redox process is chemically reversible in MeCN (0.2 M NBu_4PF_6) at 253 K.

The bulk reduction of **1** at +0.05 V versus Fc^+/Fc confirmed a one-electron reduction and resulted in the deposition of Au metal onto the surface of working electrode. A subsequent cyclic voltammogram of the electrolyzed solution confirmed decomposition of the complex and its removal from solution.

The electrochemical behavior of $[Au([9]aneS_2O)_2]^{+/2+/3+}$ in MeCN solution differs significantly from that of $[Au([9]aneS_3)_2]^{+/2+/3+}$ (Table 4). The latter complex undergoes discrete one-electron changes that can be resolved by cyclic voltammetry, whereas **1** exhibits a two-electron, chemically reversible oxidation process to generate $[Au([9]aneS_3)_2]^{3+}$ via the formation of $[Au([9]aneS_3)_2]^{2+}$ as an intermediate species.[20,40] The observation of a two-electron oxidation process for **1** implies that the potentials of the $[Au([9]aneS_2O)_2]^{3+/2+}$ and $[Au([9]aneS_2O)_2]^{2+/+}$ couples are very similar. Thus, $[Au([9]aneS_2O)_2]^{2+}$ may undergo disproportionation reactions, a conclusion supported by the isolation of crystals of **1a** from solutions of **2**.

In contrast to $[Au([9]aneS_2O)_2]^+$, $[Au([9]aneS_3)_2]^+$ is relatively unstable in solution reflecting the differences in solid-state structures of these species. In $[Au([9]aneS_2O)_2]^+$ both [9]aneS$_2$O macrocycles adopt a bidentate binding mode. However, in $[Au([9]aneS_3)_2]^+$ one [9]aneS$_3$ macrocycle binds in a monodentate mode to the Au^I center[20] making $[Au([9]aneS_3)_2]^+$ much more susceptible to decomposition in solution. Such decomposition could involve the displace-

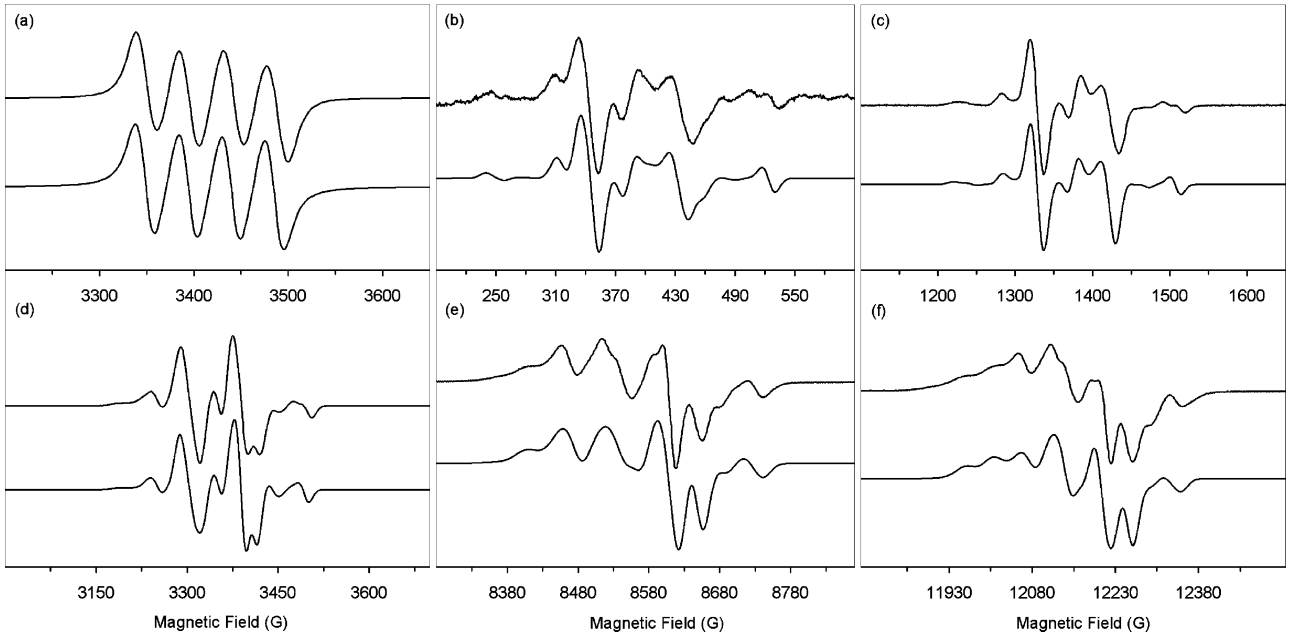

Figure 5. Multifrequency EPR spectra of $[Au([9]aneS_2O)_2]^{2+}$ in MeCN solution; (a) X-band fluid spectrum at 293 K (top) and its simulation (bottom) with $g_{iso} = 2.0182$, $|A_{iso}| = 44 \times 10^{-4}$ cm^{-1} and Gaussian line width $W_{iso} = 18$ G; (b) L-band, (c) S-band, (d) X-band, (e) K-band and (f) Q-band frozen spectra at 125 K (top) and their simulations (bottom) with $g_{xx} = 2.010$, $g_{yy} = 2.006$, $g_{zz} = 2.037$; $|A_{xx}| = |A_{yy}| = |A_{zz}| = 47 \times 10^{-4}$ cm^{-1}; $P_{xx} = -18 \times 10^{-4}$ cm^{-1}, $P_{yy} = -10 \times 10^{-4}$ cm^{-1}and $P_{zz} = +28 \times 10^{-4}$ cm^{-1} with Gaussian linewidths $W_{xx} = W_{yy} = W_{zz} = 7$ G for (b); $W_{xx} = W_{yy} = W_{zz} = 8$ G for (c); $W_{xx} = W_{yy} = 9$ G, $W_{zz} = 11$ G for (d); $W_{xx} = W_{yy} = 13$ G, $W_{zz} = 19$ G for (e), and $W_{xx} = W_{yy} = 14$ G, $W_{zz} = 21$ G for (f).

ment of the terminal thioether donor by the solvent or other species in solution. This instability of $[Au([9]aneS_3)_2]^+$ has prevented the observation of the electrochemical oxidation of this species to $[Au([9]aneS_3)_2]^{2+/3+}$ by cyclic voltammetry in MeCN solution. In addition, the irreversible reduction of $[Au([9]aneS_3)_2]^{2+}$ at $E_p^c = +0.12$ V versus Fc^+/Fc leads to the generation of unidentified Au^I species.[20,40] Observable oxidative electrochemistry for $[Au([9]aneS_3)_2]^{+/2+/3+}$ is limited to $[Au([9]aneS_3)_2]^{2+}$ which undergoes a quasi-reversible one-electron oxidation to $[Au([9]aneS_3)_2]^{3+}$ at $E_{1/2} = +0.46$ V versus Fc^+/Fc, a potential significantly less anodic than observed for the oxidation to $[Au([9]aneS_2O)_2]^{3+}$ at $E_p^a = +0.74$ V versus Fc^+/Fc, suggesting an overall stabilization of the higher oxidation state metal centers with homoleptic thioether macrocyclic co-ordination. UV-vis spectroelectrochemical studies have demonstrated that the $[Au([9]aneS_3)_2]^{2+/3+}$ conversion is chemically reversible.[20,40]

Multifrequency EPR Studies of $[Au([9]aneS_2O)_2]^{2+}$. Paramagnetic **2** was dissolved in MeCN, and the red solution was studied by multifrequency EPR spectroscopy as a fluid solution at X-band and frozen solutions (125 K) at L-, S-, X-, K- and Q-band (Figure 5). The fluid spectrum shows four evenly spaced peaks due to the hyperfine coupling to the ^{197}Au nucleus ($I = {}^3/_2$, 100% natural abundance). Simulation of this spectrum gives $g_{iso} = 2.018$ and $|A_{iso}| = 44 \times 10^{-4}$ cm^{-1} with a Gaussian line width $W_{iso} = 18$ G (Figure 5a). The frozen solution spectra at all frequencies are complicated with only the Q-band spectrum showing a partial resolution of the *g*-values confirming the rhombic nature of the *g*-matrix. Spectral simulation (see below) reveals principal *g*-values which we have assigned as $g_{xx} = 2.010$, $g_{yy} = 2.006$, and $g_{zz} = 2.037$. Following simple crystal field arguments for an approximate square-planar, formal Au^{II}

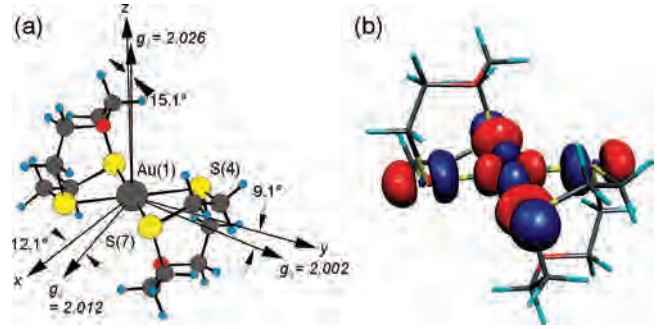

Figure 6. Co-ordinate frame used in the DFT calculations, the principal *g*-values, and the orientation of the *g*-matrix calculated with an all-electron TZP basis set at the relativistic level; (b) isosurface plot of the SOMO of $[Au([9]aneS_2O)_2]^{2+}$ for the α-spin.

d^9 complex, and by comparisons to $[Au([9]aneS_3)_2]^{2+}$,[16] we expect the SOMO in **2** to be a $5d_{xy}$ orbital where the *xy* plane is defined by the AuS_4 plane. Thus, the largest principal *g*-value (g_{zz}) lies perpendicular to the plane containing the SOMO. Within the Q-band spectra transitions of the lowest field (g_{zz}) ^{197}Au hyperfine quartet are resolved, as are those of the central (g_{xx}) feature. However, at lower frequencies this resolution is lost as the resolution in *g*-anisotropy decreases with decreasing frequency and the spectra become dominated by ^{197}Au hyperfine couplings. At L-, S- and X-band the spectra show four lines of varying relative intensity consistent with a near isotropic metal hyperfine matrix within a system exhibiting low *g*-anisotropy. The variations in intensity within the ^{197}Au quartets at each frequency are indicative of a large quadrupole coupling to the $I = {}^3/_2$ ^{197}Au nucleus which is of a similar magnitude to that of the metal hyperfine interaction.[10] We have observed similarly strong quadrupole effects during our multifrequency EPR spectroscopic studies of $[Au([9]aneS_3)_2]^{2+}$.[16]

Simulations. The spectra were simulated using the spin-Hamiltonian

$$\hat{H} = \beta_e \mathbf{g} B\hat{S} + \hat{S}\mathbf{A}\hat{I} + g_n\beta_n B\hat{I} + P_{zz}[3\hat{I}_z^2 - I(I+1)] + (P_{xx} - P_{yy})(\hat{I}_x^2 - \hat{I}_y^2)$$

where β_e and β_n are the electronic and ^{197}Au nuclear Bohr magnetons, respectively, B is the applied magnetic field, g and A are the electronic g-matrix and ^{197}Au nuclear hyperfine matrix, respectively, and P_{ii} ($i = x, y, z$) are the principal values of the nuclear quadrupole interaction tensor P, defined by

$$P_{ii} = \frac{eQq_{ii}}{4I(2I-1)} \text{ and } q_{ii} = \frac{\partial^2 V}{\partial i^2}$$

where e is the electronic charge, Q is the quadrupole moment of the ^{197}Au nucleus, and q_{ii} are the principal values of the electric field gradient at the nucleus. The P tensor is traceless; thus, its principal components can be parametrized by $P = [P_{zz} - (P_{xx} + P_{yy})/2]/3$ and a rhombic term $\eta = (P_{xx} - P_{yy})/2$. We simulated the Q-band EPR spectrum by ignoring metal quadrupole effects to provide reasonable first estimates of the principal values of the g- and A-matrices, the principal axes of which were assumed to be coincident. We set our initial estimates of the principal values of the A-matrix to $|A_{xx}| = |A_{yy}| = |A_{zz}| = 44 \times 10^{-4}$ cm^{-1} derived from $|A_{iso}| = 44 \times 10^{-4}$ cm^{-1} as determined from the fluid solution X-band EPR spectrum of **2**. To reproduce the outermost features at the low and high field regions of the Q-band spectrum we introduced quadrupole coupling terms with $P = 14 \times 10^{-4}$ cm^{-1} and $\eta = 0$. The subsequent refinement of a single set of simulated spin Hamiltonian parameters was achieved through an iterative process in which all of the L-, S-, X-, K- and Q-band spectra were simulated simultaneously; the L-, S- and X-band spectra were particularly sensitive to our refinements of the rhombic term, η. The final set of parameters derived from these simulations is $g_{xx} = 2.010$, $g_{yy} = 2.006$, $g_{zz} = 2.037$; $|A_{xx}| = 47 \times 10^{-4}$ cm^{-1}, $|A_{yy}| = 47 \times 10^{-4}$ cm^{-1}, $|A_{zz}| = 47 \times 10^{-4}$ cm^{-1}; $P_{xx} = -18 \times 10^{-4}$ cm^{-1}, $P_{yy} = -10 \times 10^{-4}$ cm^{-1}, and $P_{zz} = 28 \times 10^{-4}$ cm^{-1}. The simulated isotropic hyperfine coupling A_{iso} requires the signs of the principal components of the A-tensor to be either all positive or all negative consistent with $A_{iso} = (A_{xx} + A_{yy} + A_{zz})/3$. From our simulations and simulated linewidths we estimate errors of ± 0.001, $\pm 5 \times 10^{-4}$ cm^{-1} and $\pm 3 \times 10^{-4}$ cm^{-1} for the principal components of the g-, A-, and P-tensors, respectively, the error in A possibly accounting for the slight difference between A_{iso} determined from the simulations of the fluid and frozen solution spectra. Our simulations of the frozen solution spectra of **2** exhibit an isotropic A-matrix with a small g-anisotropy. Thus, our simulations were not particularly sensitive to non-coincidence effects and consequently we cannot comment on the relative orientations of the g-, A-, and P- tensor frames of **2** on the sole basis of our simulations of the EPR spectra. Consequently, we report spin Hamiltonian parameters for simulations in which the g-, A-, and P- tensors are coincident.

Interpretation of EPR Data of [Au([9]aneS$_2$O)$_2$]$^{2+}$. To interpret the EPR spectra of [Au([9]aneS$_2$O)$_2$]$^{2+}$ we followed a similar approach to that developed for the analogous [Au([9]aneS$_3$)$_2$]$^{2+}$ species.[16] Thus, g_{xx} and g_{yy} are assigned to orientations lying in the equatorial AuS$_4$ plane, with g_{zz} (the largest g-value) perpendicular to this plane. Crystal field theory arguments place the unpaired electron in the Au 5d$_{xy}$ orbital. DFT calculations are consistent with this interpretation, predicting that the SOMO has a$_g$ symmetry in C_i symmetry, and that the dominant metal component of the SOMO is 5d$_{xy}$ (see below). In this case, the principal components of the g and A-matrices are given by eqs 1 and 2, respectively,[43]

$$\begin{aligned} g_{xx} &= g_e + 2\delta_{xz} \\ g_{yy} &= g_e + 2\delta_{yz} \\ g_{zz} &= g_e + 8\delta_{x^2-y^2} \end{aligned} \quad (1)$$

$$\begin{aligned} A_{xx} &= A_s + P_d\left[\frac{2}{7}a^2 + \Delta g_{xx} - \frac{3}{14}\Delta g_{yy}\right] \\ A_{yy} &= A_s + P_d\left[\frac{2}{7}a^2 + \Delta g_{yy} - \frac{3}{14}\Delta g_{xx}\right] \\ A_{zz} &= A_s + P_d\left[-\frac{4}{7}a^2 + \Delta g_{zz} - \frac{3}{14}(\Delta g_{xx} + \Delta g_{yy})\right] \end{aligned} \quad (2)$$

where g_e is the free electron g-value, Δg_{ii} are the shifts of the g-values from g_e, P_d is the electron−nuclear dipolar coupling parameter for Au 5d electrons, and α is the linear combination of atomic orbitals (LCAO) coefficient of the Au 5d$_{xy}$ orbital in the SOMO. The δ_i terms are the weighted average ground state-excited state energy gaps:

$$\delta_i = \sum_{k \neq 0} \frac{\lambda c_{ik}^2}{E_0 - E_k}$$

where λ is the spin−orbit coupling constant for Au 5d electrons, and c_{ik} is the LCAO coefficient of the ith atomic orbital in the kth molecular orbital. A_S is the isotropic Fermi contact term given by

$$A_S = \langle A \rangle - P_d\left(\frac{\Delta g_{xx} + \Delta g_{yy} + \Delta g_{zz}}{3}\right) \quad (3)$$

and can include contributions from direct admixture of 6s orbital density to the SOMO and from inner core polarization.

From eqs 1 we expect g_{zz}, g_{yy}, and $g_{xx} > g_e$ with g_{zz} being the largest g-value, oriented perpendicular to the plane of the formal 5d$_{xy}$ orbital, and this is the basis of our assignment of the orientation of the z-axis (see above). Equations 1 and 2 assume that the principal axes of the g- and A-matrices are coincident, and we have assumed this to be the case experimentally because we achieve good simulations without including non-coincidence effects. However, it should be noted that this situation is not required for the C_i molecular point symmetry of [Au([9]aneS$_2$O)$_2$]$^{2+}$ because in C_i all of the 5d orbitals transform as a$_g$ and can therefore mix. This scrambling of d-orbital functions can give rise to g- and A-matrix non-coincidence effects.[43] DFT calculations (see later) suggest that the dominant contribution to the SOMO is 5d$_{xy}$ (27.2%) and that there are negligible contributions from the other 5d orbitals of a$_g$ symmetry. Thus, non-coincidence effects in **2** are likely to be minor.

(43) Rieger, P. H. *Cood. Chem. Rev.* **1994**, *135*, 203–286.

Table 5. 5d Contribution to the EFG from Mulliken Population Analyses

	$\langle 3\cos^2\theta - 1\rangle$	Free ion population (n_i)	$n_i\langle 3\cos^2\theta - 1\rangle$	AuS_4O_2 population (n_i)[a]	$n_i\langle 3\cos^2\theta - 1\rangle$
Au $5d_{x^2-y^2}$	−4/7	2	−8/7	1.96	−1.12
Au $5d_{xy}$	−4/7	1	−4/7	1.69	−0.97
Au $5d_{xz}$	2/7	2	4/7	1.98	0.57
Au $5d_{yz}$	2/7	2	4/7	1.98	0.57
Au $5d_{z^2}$	4/7	2	8/7	1.98	1.13
Sum		9	0.57	9.59	0.18
$\langle r^{-3}\rangle\sum n_i\langle 3\cos^2\theta-1\rangle$/a.u.			8.91		2.82
covalency reduction factor			1.00		0.32
$P_{zz}/10^{-4}$ cm^{-1}			67		21

[a] Mulliken populations from DFT calculations using TZP basis set.

A combination of eqs 1−3 gives

$$A_{zz} = \langle A\rangle - P_d\left[-\frac{4}{7}a^2 + \frac{2}{3}\Delta g_{zz} - \frac{5}{42}(\Delta g_{xx} + \Delta g_{yy})\right] \quad (4)$$

Clearly a strictly isotropic hyperfine interaction would imply zero d-orbital contribution to the SOMO. However, even a small anisotropy of 1×10^{-4} cm^{-1} would give a value of $a^2 \approx 0.07$, because P_d for ^{197}Au is small (deriving from the small nuclear magnetic moment). Hence for **2** we can only put an upper limit on α^2 based on our estimated uncertainties in A_{ii}: solution of eq 4 with a maximum $A_{zz} - \langle A\rangle$ from our estimated errors in A_{ii} ($\pm 5 \times 10^{-4}$ cm^{-1}) places an upper limit of $\alpha^2 = 0.28$ for the LCAO coefficient.

The C_i point symmetry of $[Au([9]aneS_2O)_2]^{2+}$ also allows direct admixture of the Au 6s orbital in to the a_g SOMO, and this could give rise to the relatively large isotropic component of the *A*-matrix. This can be estimated directly from the ratio of the experimental isotropic hyperfine A_{iso} (44×10^{-4} cm^{-1}) and the calculated hyperfine coupling for unit population of the 6s orbital in the $5d^86s^1$ configuration, $A_{6s} = 1874 \times 10^{-4}$ cm^{-1},[44] to give about 2−3% Au 6s contribution to the SOMO although this should be viewed as an upper limit because spin polarization of inner core s-electrons can also contribute to the observed isotropic hyperfine.

Quadrupole Interactions. Our previous studies of $[Au([9]aneS_3)_2]^{2+}$, together with those of $[Au(mnt)_2]^{2-}$, $[Au(dmit)_2]^{2-}$ and $[Au(dtc)_2]$ demonstrate that quadrupole interactions can be significant in complexes possessing a formal Au^{II} center.[16] These effects arise from an anisotropic electron density distribution and the resulting electric field gradients (EFG) at the Au^{II} nucleus. For Au^{II} complexes the nuclear quadrupole can be of similar magnitude to the metal hyperfine interaction which can result in perturbations of the intensity and in the spacing of $\Delta m_I = 0$ transitions.[16] In our study of $[Au([9]aneS_3)_2]^{2+}$, we showed that a rhombic η parameter and a single angle of non-coincidence between *P* and *A* were required to reproduce the irregular spacings of the four ^{197}Au hyperfine components of the g_{zz} and g_{yy} quartets in the EPR spectra.[16] For $[Au([9]aneS_2O)_2]^{2+}$, non-coincidence effects were not apparent in the frozen solution EPR spectra; however, *P* and a nonzero rhombic η parameter had to be incorporated into the model for the satisfactory simulation of the spectra at L-, S-, X-, K- and Q-band frequencies with those simulations of the L-, S- and X-band spectra being particularly sensitive to η.

Belford has used Mulliken population analyses based on MO calculations to estimate the metal valence contributions to the EFG[45,46] and we have used this methodology for $[Au([9]aneS_3)_2]^{2+}$ using Mulliken population analyses derived from DFT calculations.[16] Application of the same approach to $[Au([9]aneS_2O)_2]^{2+}$, using the results of DFT calculations employing TZP basis sets for all atoms (see below), leads to a covalency reduction factor of 0.32 and a calculated $P_{zz} = 21 \times 10^{-4}$ cm^{-1}, Table 5. This is significantly smaller than the experimentally determined value ($P_{zz} = 28 \times 10^{-4}$ cm^{-1}) and suggests that we require a ligand contribution of about 7×10^{-4} cm^{-1} to augment the 5d orbital-occupancy contributions. Thus, the electron densities associated with the ligand donor atoms contribute significantly to the EFG at the Au^{II} nucleus in addition to the unequal populations of the valence 5d orbitals at the metal center.

DFT Calculations for $[Au([9]aneS_2O)_2]^{2+}$. The experimental and calculated structural parameters for the AuS_4O_2 co-ordination sphere of a model of $[Au([9]aneS_2O)_2]^{2+}$ are compared in Table 2, and the atom numbering scheme and co-ordinate frame employed in the calculations is shown in Figure 6a. The ZORA SR DFT calculations employed all-electron TZP basis sets derived from the ZORA/TZP database of the ADF suite of programs. We have shown for $[Au([9]aneS_3)_2]^{2+}$ that this level of calculation reproduces the principal features of the geometric and electronic structures of $[Au([9]aneS_3)_2]^{2+}$.[16] For $[Au([9]aneS_2O)_2]^{2+}$, the calculations reveal Au(1)−S(4) and Au(1)−S(7) distances that are 0.10 and 0.06 Å longer, respectively, than those in the experimentally determined structure of $[Au([9]aneS_2O)_2]^{2+}$ in **2a** and S(4)−Au(1)−S(4) bond angles that are about 2° smaller. The asymmetry of the Au(1)−S(4) and Au(1)−S(7) distances, revealed by X-ray crystallography, is also reflected in the DFT geometry optimized structure of $[Au([9]aneS_2O)_2]^{2+}$. However, the asymmetry between these distances in the calculated structure appears smaller (0.02 Å) than that observed for the experimentally determined structure (0.06 Å). The approximately axial Au(1)···O(1) interactions are significantly longer (0.16 Å) than those in

(44) Rieger, P. H. *J. Magn. Reson.* **1997**, *124*, 140–146.

(45) White, L. K.; Belford, R. L. *Chem. Phys. Lett.* **1976**, *37*, 553–555.

(46) White, L. K.; Belford, R. L. *J. Am. Chem. Soc.* **1976**, *98*, 4428–4438.

Table 6. Experimental and Calculated *g*-Matrix Components for $[Au([9]aneS_2O)_2]^{2+}$ and $[Au([9]aneS_3)_2]^{2+}$[16]

	$[Au([9]aneS_2O)_2]^{2+}$		$[Au([9]aneS_3)_2]^{2+}$	
	experimental (EPR)	BP-TZP SO all electron	experimental (EPR)	BP-TZP SO all electron
g_{zz}	2.037	2.026	2.032	2.031
g_{xx}	2.010	2.012	1.999	2.001
g_{yy}	2.006	2.002	1.984	1.967
Δg_{zz}/ppt	35	24	30	29
Δg_{xx}/ppt	8	10	−3	−1
Δg_{yy}/ppt	4	0	−18	−35

the experimental structure although the angle between the Au(1)···O(1) and the *z*-axis perpendicular to the AuS_4 plane is of the same order of magnitude in the calculated (23.5°) and experimental structures (20.2°) of $[Au([9]aneS_2O)_2]^{2+}$. These observations, together with the ability of the DFT calculations to reproduce the principal differences between the geometric structures of $[Au([9]aneS_2O)_2]^{2+}$ and $[Au([9]aneS_3)_2]^{2+}$, suggest that these DFT calculations are of sufficient quality to permit a qualitative understanding of the electronic properties of $[Au([9]aneS_2O)_2]^{2+}$.

The calculated SOMO for $[Au([9]aneS_2O)_2]^{2+}$ (Figure 6b) is composed of 27.2% Au $5d_{xy}$ and 64.4% equatorial S 3p character. A comparison between the experimental and calculated *g*-matrix components is presented in Table 6 showing deviations between the calculated and experimental *g*-matrix of −11, 2, and −4 ppt for g_{zz}, g_{xx}, and g_{yy}, respectively. We and others have reported similar deviations between experimental and calculated *g*-matrix components which are ascribed to over- and underestimations in the contributions from the second-order spin−orbit/orbital term in the calculated *g*-matrix.[16,47−50] Thus, the reproduction of the trends in the metrical parameters for the AuS_4O_2 co-ordination sphere, the consistency between the calculated Au contribution to the SOMO and the upper limit derived from the EPR experiments, and the similarity between the calculated and experimental *g*-matrix components support a SOMO in $[Au([9]aneS_2O)_2]^{2+}$ that possesses about 27% Au $5d_{xy}$ character. The orientation of the principal *g*-values with respect to the molecular frame is shown in Figure 6a. The largest principal *g*-value (g_{zz}) is approximately perpendicular to the *xy* plane, as expected for a formal $5d_{xy}$ SOMO, and lies 15.1° off the *z*-axis. The remaining principal *g*-values, g_{xx} and g_{yy} are 12.1° and 9.1° away from the *x* and *y* axes, respectively.

Comparison of the $[Au([9]aneS_2O)_2]^{2+}$ with $[Au([9]aneS_3)_2]^{2+}$ and $\{Au^{II}S_4\}$ Species. Summaries of principal g_{ii}-, ^{197}Au A_{ii}-, P_{ii}-, *P*-, and η-values for $[Au([9]aneS_2O)_2]^{2+}$ and $[Au([9]aneS_3)_2]^{2+}$ together with those for other formal Au^{II} thio-ligand complexes ($[Au(mnt)_2]^{2-}$, $[Au(dmit)_2]^{2-}$, and $[Au(dtc)_2]$) are presented in Table 7. $[Au(mnt)_2]^{2-}$, $[Au(dmit)_2]^{2-}$, and $[Au(dtc)_2]$ possess significantly delocalized ground states involving S π-interactions and, for $[Au(mnt)_2]^{2-}$ and $[Au(dmit)_2]^{2-}$, significant π-contributions from the C=C ligand backbones. The spin Hamiltonian parameters for these complexes are all very similar and reflect the similarity in their electronic structures. Some of these spin Hamiltonian parameters are similar to those for $[Au([9]aneS_2O)_2]^{2+}$ (P_{ii}) and $[Au([9]aneS_3)_2]^{2+}$ (g_{ii}) whereas the metal hyperfines (A_{ii}) are consistently smaller mirroring a lower Au-contribution and greater delocalization in the SOMOs in $[Au(mnt)_2]^{2-}$, $[Au(dmit)_2]^{2-}$, and $[Au(dtc)_2]$ when compared to $[Au([9]aneS_2X)_2]^{2+}$ (X = O, S, Table 7).

The *g*-values of $[Au([9]aneS_2O)_2]^{2+}$ are less rhombic than those of $[Au([9]aneS_3)_2]^{2+}$ and approach an axial symmetry with g_{ii} ($i = x, y, z$) > g_e consistent with the metal-based first order perturbation treatment of the spin−orbit coupling described in eqs 1 and for the essentially square planar geometry of the AuS_4 unit in $[Au([9]aneS_2O)_2]^{2+}$. $[Au([9]aneS_3)_2]^{2+}$ possesses significant negative contributions to the *g*-shifts that arise from low energy charge-transfer transitions from predominantly ligand-based orbitals.[16] Such low energy charge-transfer transitions have been observed to give rise to negative *g*-shifts in several $\{Au^{II}S_4\}$ complexes.[4,6,7,9,10,51,52] Given the similar nature of the SOMOs of $[Au([9]aneS_2X)_2]^{2+}$ (Au $5d_{xy}$ character up to 27 and 30% for X = O, S, respectively) and the similar Au−S bond distances in the AuS_4 planes of $[Au([9]aneS_2O)_2]^{2+}$ and $[Au([9]aneS_3)_2]^{2+}$ (Tables 2 and 3), it is likely that these negative contributions are associated with ligand-to-metal charge transfer (LMCT) between the axial S-donors and the Au^{II} center in $[Au([9]aneS_3)_2]^{2+}$, which is absent in $[Au([9]aneS_2O)_2]^{2+}$. The essentially isotropic ^{197}Au hyperfine *A*-values in $[Au([9]aneS_2O)_2]^{2+}$ are also consistent with a lower rhombicity in $[Au([9]aneS_2O)_2]^{2+}$ when compared to $[Au([9]aneS_3)_2]^{2+}$ and with a lower ^{197}Au contribution to the SOMO in $[Au([9]aneS_2O)_2]^{2+}$ (Au $5d_{xy}$ ca. 27% when estimated experimental errors in the simulated *A*-values are included in the calculation).

The nuclear quadrupole parameters of $[Au([9]aneS_2X)_2]^{2+}$ (X = O, S, Table 7) are very sensitive to the nature of the co-ordination sphere about the Au^{II} center with those of $[Au([9]aneS_2O)_2]^{2+}$ ($P = 14.0 \times 10^{-4}$ cm^{-1}, $\eta = -2.6 \times 10^{-4}$ cm^{-1}) being much nearer axial than those of $[Au([9]aneS_3)_2]^{2+}$ which are essentially rhombic ($P = 5.0 \times 10^{-4}$ cm^{-1}, $\eta = 5.0 \times 10^{-4}$ cm^{-1}). In addition, P_{zz} for $[Au([9]aneS_2O)_2]^{2+}$ (28×10^{-4} cm^{-1}) is significantly greater than that for $[Au([9]aneS_3)_2]^{2+}$ (10×10^{-4} cm^{-1}) reflecting a greater EFG along the molecular *z*-axis in $[Au([9]aneS_2O)_2]^{2+}$ when compared to $[Au([9]aneS_3)_2]^{2+}$. Our comparisons of the 5d valence electron contributions to P_{zz} and the experimentally determined P_{zz} indicate that there are significant contributions to the EFG derived from the electron density associated with the ligands in $[Au([9]aneS_2O)_2]^{2+}$. Thus, the difference in P_{zz} for $[Au([9]aneS_2X)_2]^{2+}$ (X = O, S, Table 7) is consistent with a more asymmetric electron density in $[Au([9]aneS_2O)_2]^{2+}$ as indicated by the

(47) Patchkovskii, S.; Ziegler, T. *J. Chem. Phys.* **1999**, *111*, 5730–5740.
(48) Patchkovskii, S.; Ziegler, T. *J. Am. Chem. Soc.* **2000**, *122*, 3506–3516.
(49) Stein, M.; van Lenthe, E.; Baerends, E. J.; Lubitz, W. *J. Phys. Chem. A* **2001**, *105*, 416–425.
(50) van Lenthe, E.; van der Avoird, A.; Hagen, W. R.; Reijerse, E. J. *J. Phys. Chem. A* **2000**, *104*, 2070–2077.
(51) Kampf, M.; Griebel, J.; Kirmse, R. *Z. Anorg. Allg. Chem.* **2004**, *630*, 2669–2676.
(52) van Rens, J. G. M.; Viegers, M. P. A.; de Boer, E. *Chem. Phys. Lett.* **1974**, *28*, 104–108.

Table 7. Comparison of Spin-Hamiltonian Parameters of Mononuclear Au(II) Compounds

	$[Au(mnt)_2]^{2-}$ [c]	$[Au(dmit)_2]^{2-}$ [d]	$[Au(dtc)_2]$ [e]	$[Au([9]aneS_2O)_2]^{2+}$	$[Au([9]aneS_3)_2]^{2+}$ [f]
g_{xx} [a]	2.006	2.002	2.008	2.010	1.999
g_{yy}	1.978	1.982	1.986	2.006	1.980
g_{zz}	2.016	2.042	2.118	2.037	2.032
A_{xx} [b]	−41	−40	−32	−47	−50
A_{yy}	−39	−39	−32	−47	−30
A_{zz}	−42	−41	−30	−47	−50
P_{xx} [b]	−7	−6	−19	−18	0
P_{yy}	−19	−17	−9	−10	−10
P_{zz}	+26	+23	+28	+28	+10
P	13.0	11.5	14.0	14.0	5.0
η	6.0	5.5	−5.0	−2.6	5.0

[a] z axis is perpendicular to AuS_4 plane, y bisects S−Au−S chelate angles. [b] Diagonal elements A_{ii}, P_{ii} and P and η in 10^{-4} cm^{-1}. [c] See ref 7. [d] See ref 9. [e] See ref 10. P_{ii} elements have been multiplied by 2 from the values given in ref 10 to be consistent with the definition in this work. [f] See ref 16. [g] mnt = maleonitriledithiolate, dmit = dimercaptoisotrithione, dtc = diethyldithiocarbamate, [9]aneS$_3$ = 1, 4, 7-trithiacyclononane.

Mulliken charges derived from the DFT calculations for each donor atom in the coordination sphere. The equatorial S-donors in each $[Au([9]aneS_2X)_2]^{2+}$ possess similar Mulliken charges [S(4) = 0.32, S(7) = 0.33 and S(4) = 0.31, S(7) = 0.31 for X = O, S respectively]. In $[Au([9]aneS_3)_2]^{2+}$ the axial S(1) donor possesses a slightly lower Mulliken charge (0.20) than the equatorial S atoms; however, in $[Au([9]aneS_2O)_2]^{2+}$ the axial O(1) donor possesses a Mulliken charge (−0.55) that is significantly lower than and of opposite sign to those of the equatorial S atoms. The distribution and relative magnitudes of these charges suggest that the asymmetry in the electron density lies approximately along the z-axis (Figure 6) and perpendicular to the equatorial plane. In addition, the nuclear quadrupole parameters for $[Au([9]aneS_2O)_2]^{2+}$ are of a similar magnitude to the approximately square-planar $[Au(mnt)_2]^{2-}$,[7] $[Au(dmit)_2]^{2-}$,[9] and $[Au(dtc)_2]$[10] complexes (Table 7) consistent with the X-ray crystallographic studies of $[Au([9]aneS_2O)_2]^{2+}$ which reveals a co-ordination geometry that may be viewed as a distorted AuS_4 square plane with distant O donors occupying the axial positions (see above).

Conclusions

The mononuclear Au^I, Au^{II}, and Au^{III} complexes $[Au([9]aneS_2O)_2]^{+/2+/3+}$ have been prepared as **1**, **2**, and **3** and structurally characterized by X-ray crystallography as $[Au^I([9]aneS_2O)_2]BF_4 \cdot MeCN$, $[Au^{II}([9]aneS_2O)_2](BF_4)_2 \cdot 2MeCN$, and $[Au^{III}([9]aneS_2O)_2](ClO_4)_6(H_5O_2)(H_3O)_2$, respectively. Our structural studies reveal significant differences within the co-ordination spheres of $[Au([9]aneS_2O)_2]^{+/2+/3+}$ when compared to their $[Au([9]aneS_3)_2]^{+/2+/3+}$ counterparts reflecting the preference for soft−soft Lewis acid−base interactions involving Au and S in these complexes. The differences within the co-ordination spheres of these complexes are manifested in significantly different electrochemical behaviors and electronic structures for the complexes $[Au([9]aneS_2X)_2]^{2+}$ (X = O, S). Multifrequency EPR studies of $[Au^{II}([9]aneS_2O)_2]^{2+}$ are consistent with a center exhibiting lower rhombicity and a larger axial quadrupole coupling to a ^{197}Au nucleus than for the related $[Au^{II}([9]aneS_3)_2]^{2+}$ center,[16] with the quadrupole coupling parameters being particularly sensitive to these changes in the co-ordination sphere. The interpretation of spin Hamiltonian parameters together with supporting DFT calculations show that the SOMO of $[Au([9]aneS_2O)_2]^{2+}$ has up to 27% Au $5d_{xy}$ character which is slightly less than that for $[Au([9]aneS_3)_2]^{2+}$ (ca. 30% Au $5d_{xy}$ character).[16]

Acknowledgment. We thank the EPSRC and the University of Nottingham for support and funding. D.H. gratefully acknowledges receipt of the Madam Chen Zhili Fellowship. We thank the EPSRC *cw*-EPR Service at The University of Manchester. M.S. gratefully acknowledges receipt of a Royal Society Wolfson Merit Award and of a Leverhulme Trust Senior Research Fellowship.

Supporting Information Available: The geometry optimized co-ordinates of $[Au([9]aneS_2O)_2]^{2+}$ derived from the DFT calculations are available as Supporting Information. X-ray crystal data are available in Crystallographic Information File (CIF) format. This material is available free of charge via the Internet at http://pubs.acs.org.

IC8010037